Laplace-transform analytic-element method for transient porous-media flow

Kristopher L. Kuhlman · Shlomo P. Neuman

Abstract   A unified theory of the Laplace-transform analytic-element method (LT-AEM) for solving transient porous-media flow problems is presented. LT-AEM applies the analytic-element method (AEM) to the modified Helmholtz equation, the Laplace-transformed diffusion equation. LT-AEM uses superposition and boundary collocation with Laplace-space convolution to compute flexible semi-analytic solutions from a small collection of fundamental elements. The elements discussed are derived using eigenfunction expansions of element shapes in their natural coordinates. A new formulation for a constant-strength line source is presented in terms of elliptical coordinates and complex-parameter Mathieu functions. Examples are given illustrating how leaky and damped-wave hydrologic problems can be solved with little modification using existing LT-AEM techniques.

Keywords   Analytic element · Diffusion equation · Elliptical coordinates · Laplace transform · Mathieu functions · Modified Helmholtz equation · Transient line source

Abbreviations
AEM   Analytic-element method
LT-AEM   Laplace-transform analytic-element method

1 Introduction

The analytic-element method (AEM) provides semi-analytic solutions to linear porous-media flow problems through superposition of fundamental solutions. The original development of AEM is due to Strack and his co-workers at the University of Minnesota [1]. During its initial development, it was compared to the boundary-element method [2], but the eigenfunction-expansion approach discussed here may be considered a special case of the spectral method (see [3, Sect. 3.1] and [4, Appendix C]). Each AEM element satisfies the governing equation, while spectral elements typically do not. The majority of AEM applications to date have been concerned with vertically averaged steady-state groundwater flow (the two-dimensional (2D) Laplace and Poisson equations in the horizontal plane). AEM has been extended to three-dimensional [5], transient [6], multi-layer [7], and linearized unsaturated [8] flow

K. L. Kuhlman (✉) · S. P. Neuman
Department of Hydrology and Water Resources, University of Arizona, Tucson, AZ 85721, USA
e-mail: klkuhlm@sandia.gov

problems. Review papers [9–11] and textbooks by Strack [12] and Haitjema [13] cover the fundamentals, discuss applications, and mention some recent advances.

AEM partially fills a gap between analytic solutions derived for simple geometries (e.g. radially symmetric flow to a well) and distributed-parameter gridded models (e.g. finite-element methods). AEM is well-suited for time-independent boundary-value problems; applications to transient diffusion have proceeded in several directions.

The earliest extension of AEM to transient flow [14] was discontinuous in time, using a grid to simulate transient storage. The corresponding space discretization offset the mesh-free benefit normally associated with AEM. Another early approach [15] combined steady and transient elements, using line and area sources to model transient effects; transient storage effects were assumed piecewise-constant in time and the method required zero net withdrawal of water from the aquifer. While not an AEM solution, Butler and Liu [16] developed a solution for transient flow to a well in the presence of a single circular inhomogeneity, using an approach similar to that taken here. Bakker [17] used a temporal Fourier transform to apply the AEM to problems comprised of a finite number of temporal harmonics. Strack [18] described a general AEM approach in which localized transient perturbation elements are superimposed on a confined steady background that uses finite differences in time.

Furman and Neuman [6] first used AEM to solve the Laplace-transformed diffusion equation. LT-AEM numerically back-transforms the solution into the time domain using an inverse-Laplace-transform algorithm. In contrast to the Fourier-transform approach, the use of the Laplace transform obviates the need for periodicity and can incorporate initial conditions. We illustrate LT-AEM elements constructed using eigenfunction expansion and Laplace-space convolution. Steady-state multi-layer aquifer systems [7] and linearized steady unsaturated flow [19,20] also lead to the Helmholtz equation. We show how these types of homogeneous distributed sources can be incorporated into the LT-AEM. The elements outlined here are restricted to simple geometries (i.e., circles and ellipses), but other techniques (e.g. those utilized in spectral-element modeling [3, Chap. 17]) can be used to extend LT-AEM to more general geometries.

2 Laplace-transform AEM

Hydraulic head in a transient, 2D, confined, elastic aquifer is described by the diffusion equation,

$$Kb\nabla^2 h(\mathbf{x}, t) + bG = bS_s \frac{\partial h(\mathbf{x}, t)}{\partial t}, \tag{1}$$

where $h(\mathbf{x}, t)$ is the vertically averaged hydraulic head $[L]$, b is the aquifer thickness $[L]$, G is a volumetric source term $[1/T]$, K is the hydraulic conductivity $[L/T]$, and S_s is the specific storage $[1/L]$. K is assumed isotropic; both K and S_s are assumed homogeneous. For horizontal 2D flow, a unit aquifer thickness is assumed for simplicity (unless stated otherwise), without loss of generality. 2D vertical-plane flow could also be simulated with this approach, e.g. flow under a wide dam on a permeable foundation.

In AEM it is standard to work with a discharge potential $[L^3/T]$, $\Phi = bKh + C$, where C is an arbitrary reference [12] that we conveniently set to zero. Applying the Laplace transform [21, Chap. 4] to (1), written in terms of Φ, with $G = 0$, we have

$$\alpha\nabla^2\bar{\Phi}(\mathbf{x}) = \bar{\Phi}(\mathbf{x})p - \Phi_0, \tag{2}$$

where $\alpha = K/S_s$ is the hydraulic diffusivity $[L^2/T]$, p is the Laplace-transform parameter $[T^{-1}]$, $\bar{\Phi}(\mathbf{x})$ is the transformed discharge potential $[L^3]$, and Φ_0 is the initial value of Φ. To render (2) homogeneous, we set $\Phi_0 = 0$; non-zero initial conditions are introduced using impulse area sources at $t = 0$ [22]. The governing equation in Laplace space is the Yukawa [23] or modified Helmholtz equation

$$\nabla^2\bar{\Phi}(\mathbf{x}) - \kappa^2\bar{\Phi}(\mathbf{x}) = 0, \tag{3}$$

where $\kappa^2 = p/\alpha$ $[L^{-2}]$ is analogous to the wave number in wave-propagation problems [24, Sect. 1.1.2], or alternatively $\kappa = 1/(Z_0 K)$, where Z_0 is the mechanical analog of impedance [25, Chap. 7].

2.1 Laplace-space convolution

Duhamel's theorem [26, Chap. 5] states that temporal behavior of a function can be obtained from convolution of the impulse response, $\Phi_{\text{imp}}(\mathbf{x}, t)$, and a time behavior, $g(t)$, through the convolution integral

$$\Phi_{\text{gen}}(\mathbf{x}, t) = \int_0^t \Phi_{\text{imp}}(\mathbf{x}, t - \tau) g(\tau) \, d\tau. \tag{4}$$

LT-AEM elements are derived in Laplace space where (4) becomes

$$\bar{\Phi}_{\text{gen}}(\mathbf{x}, p) = \bar{\Phi}_{\text{imp}}(\mathbf{x}, p) \bar{g}(p). \tag{5}$$

When convolution is performed in the time domain [15], each different time behavior (e.g. constant, pulse, or linearly increasing in time) requires approximation of (4). LT-AEM allows for separate handling of the time ($\bar{g}$) and space ($\bar{\Phi}_{\text{imp}}$) behavior of elements through the numerical inverse Laplace transform.

Many useful $\bar{g}(p)$ functions can be found tabulated in the literature (e.g. [27, Chap. 29], [21, Appendix A], and [26, Sect. 7.3]); piecewise linear or constant functions can be used to describe fairly general behavior. While it would be possible to perform the convolution in the time domain, we expect that this increases the required effort. The time-domain convolution integral (4) requires integrating $0 \leq \tau \leq t$, essentially equivalent to time-marching required by an initial-value problem (e.g. explicit finite differences in time).

2.2 Boundary matching

Elements are mathematical entities that represent physical objects in the flow system. AEM and LT-AEM use non-intersecting elements to represent areas of differing properties and source terms (see Fig. 1), by enforcing head and normal flux continuity along the element boundaries. Each LT-AEM element is derived with implied zero initial condition and zero effect at large distance. The elements in Fig. 1 will be used as an example, 2 point sources of prescribed strength and 3 circular regions of different K with unknown strengths. Head matching consists of setting

$$\bar{h}_{\text{tot}}^+(r_{n0}) = \bar{h}_{\text{tot}}^-(r_{n0}), \tag{6}$$

the total head, $\bar{h}_{\text{tot}}^{\pm} = \sum_k \bar{h}_k^{\pm}$, interior ($-$) and exterior ($+$) to the element boundary being set equal along the boundary of element n, $r_n = r_{n0}$. Head matching along the circumference of element 2 is expressed in terms of $\bar{\Phi}$ as

$$\frac{1}{K_0} \left[\bar{\Phi}_2^+ + \bar{\Phi}_1^+ + \bar{\Phi}_4 \right]_{r_{20}} = \frac{1}{K_2} \left[\bar{\Phi}_2^- + \bar{\Phi}_3^+ \right]_{r_{20}}, \tag{7}$$

where the subscript indicates a local coordinate system, and the super-scripted sign indicates the side of a two-sided element. Point source Q_5 and the insides of circles 1 and 3 do not appear in this expression, as they are neither immediately internal nor external to element 2. This convention is used by other AEM applications that solve the modified Helmholtz equation [19,28] and is equivalent to the non-overlapping domain decomposition approach called substructuring [29]; it allows regions with different coefficients in the governing equation to be matched, since they cannot be combined by superposition.

Flux matching applies to the same elements as head matching and consists of setting

$$\mathbf{n}_n \cdot \bar{\mathbf{q}}_{\text{tot}}^+(r_{n0}) = \mathbf{n}_n \cdot \bar{\mathbf{q}}_{\text{tot}}^-(r_{n0}), \tag{8}$$

Fig. 1 Example with 3 circular elements with different K (background K_0) and 2 prescribed point sources, Q_4 and Q_5
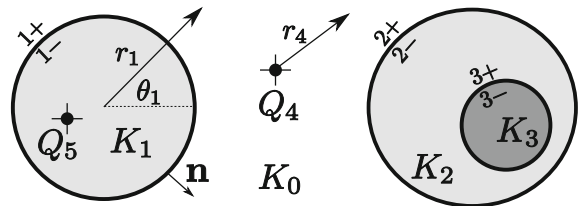
where $\mathbf{n}_n$ is the unit boundary normal for element n and $\bar{\mathbf{q}} = -\nabla\bar{\Phi}$ is the Darcy flux; the total normal flux, $\mathbf{n} \cdot \bar{\mathbf{q}}_{\text{tot}}^{\pm} = \sum_k \mathbf{n} \cdot \bar{\mathbf{q}}_k^{\pm}$, is balanced along the boundary of element n. For element 2 in Fig. 1, in terms of $\bar{\Phi}$, this yields

$$\left[\frac{\partial\bar{\Phi}_2^+}{\partial r_2} + \frac{\partial\bar{\Phi}_1^+}{\partial r_1}J_{r_1r_2} + \frac{\partial\bar{\Phi}_1^+}{\partial\theta_1}J_{\theta_1r_2} + \frac{\partial\bar{\Phi}_4}{\partial r_4}J_{r_4r_2}\right]_{r_{20}} = \left[\frac{\partial\bar{\Phi}_2^-}{\partial r_2} + \frac{\partial\bar{\Phi}_3^+}{\partial r_3}J_{r_3r_2} + \frac{\partial\bar{\Phi}_3^+}{\partial\theta_3}J_{\theta_3,r_2}\right]_{r_{20}}, \qquad (9)$$

where $J_{\theta_1r_2} = \frac{\partial\theta_1}{\partial x}\frac{\partial x}{\partial r_2} + \frac{\partial\theta_1}{\partial y}\frac{\partial y}{\partial r_2}$ is a Jacobian relating derivatives in two coordinate systems. Each of these coordinate derivatives in the Jacobian can be computed explicitly from the geometry of the elements. $\bar{\Phi}$ for each element is defined in terms of a local coordinate system (corresponding to the one used in separation of variables); differentiation with respect to local coordinates (e.g. $\partial\bar{\Phi}_2^+/\partial r_2$) leads to more concise expressions than working with a single set of coordinates everywhere.

2.3 Solution for coefficients

The modified Helmholtz equation (3) involves 2 or 3 independent variables (depending on the dimension, D). The eigenfunction expansion solution is the tensor product of the solutions obtained through separation of variables [3],

$$\bar{\Phi}_k^{\pm}(\mathbf{x}) = \prod_{i=1}^{D}\bar{\Phi}_k^{\pm}(x_i), \qquad (10)$$

where $\bar{\Phi}_k^{\pm}(x_i)$ is a sum of eigenfunctions for the coordinate x_i and element k. The orthogonal eigenfunctions here are special functions (e.g. Bessel [30, Chap. 6–8], Mathieu [31, Chap. 9] and other [32] functions). $\bar{\Phi}$ is expanded in eigenfunctions along element boundaries; the solution is then computed on or away from the boundaries using the coefficients determined from the boundary expansion. The second-order ordinary differential equations used here have solutions of the form,

$$\bar{\Phi}_k^{\pm}(x_i) = \sum_{j=0}^{N-1} a_j^{k\pm}\,\phi_j(x_i) + b_j^{k\pm}\,\psi_j(x_i) + R_N^k, \qquad (11)$$

where $\phi_j(x_i)$ and $\psi_j(x_i)$ are the eigenfunctions associated with the jth eigenvalue and coordinate x_i; $a_j^{k\pm}$ and $b_j^{k\pm}$ are free coefficients $[L^3]$ to be determined for the $\pm$ side of element k. The residual, R_N, arises from truncating the infinite expansion. Upon recombination of the solutions corresponding to the different coordinate variables (10) products of coefficients are consolidated.

Equations (10) and (11) constitute an exact expression for $\bar{\Phi}_k^{\pm}$, since $R_N^k \to 0$ as $N \to \infty$ in a least-squares sense [33, pp. 726–729] if the eigenfunctions form a complete set. Convergence is at least $\mathcal{O}(N^{-2})$ for smooth functions with continuous first derivatives [3, Sect. 2.3]. The condition of smoothness is not overly restrictive for physical problems. In cases where discontinuous functions must be expanded (e.g. intersecting or touching elements), convergence will be degraded, but the situation can often be improved with series transformation [34] or smoothing [35, Sect. 49] techniques.

Elements either have specified strength (a_j^k and b_j^k are prescribed) or they have total head or flux specified in a way which depends on the strength of other elements. LT-AEM requires three steps to compute head or flux. The first step solves for the coefficients of the eigenfunctions using boundary collocation, based on a desired arrangement of elements, source terms, and material properties. The solutions to (11) that arise in the current coordinate system are substituted in (10) at matching points along the element boundaries to obtain expressions for the coefficients of the elements. In problems with multiple elements, the coefficients must be either estimated iteratively (a fixed-point iteration over all elements) or using a direct matrix formulation. The second step evaluates the solution at the desired $\mathbf{x}$ and p, using the coefficients. Once the Laplace-space solution and its derivatives have been computed, the third step computes the time-domain solution for head and flux at each location using a numerical inverse-Laplace-transform algorithm.

2.4 LT-AEM in relation to AEM

Although conceptually LT-AEM is an application of AEM to (3), the implementation is different in several respects. Since (3) contains p, which is complex, the special functions that satisfy (11) have complex arguments or parameters. Although some inverse Laplace-transform methods only require real p, they are usually less successful at inverting discontinuous time behaviors (e.g. [36, Chap. 9] and [37, Chap. 19]), unless the calculations are performed using very high numerical precision [38].

Steady 2D AEM traditionally utilize the complex potential formulation, $\Omega = \Phi + i\Psi$ (where Ψ is a stream function), based on the Cauchy–Riemann relations. In LT-AEM both $\bar{\Phi}$ and $\bar{\Psi}$ are complex, hence this convention is not applicable, although there are analogous Cauchy–Riemann expressions for the modified Helmholtz equation if Φ and Ψ are real-valued [23]. For steady flow Ψ coincides with particle traces, but in transient problems streamlines and pathlines are generally different.

For steady 2D AEM, an important distinction is made between elements which have an effect at "infinity" and those which do not (functions of Ω with and without a branch cut) [12, Sect. 19]. LT-AEM elements are derived considering that at finite time there is no effect at ∞, which simplifies derivation and implementation. In the limit as $t \to \infty$ ($p \to 0$), these elements would have effects at infinite distance (as $p \to 0$, Eq. 3 becomes the Laplace equation). Therefore, in LT-AEM there are no branch cuts to consider or far-field fixed heads that must be set to obtain a solution, as is required for several common elements in 2D steady-state AEM.

Lastly, LT-AEM can readily be modified to handle certain distributed source terms. Analogous source terms for $\nabla^2\Phi = 0$ also lead to the Helmholtz equation [7,19,20], but would require a significant change in the solution approach. Leakance and transient effects must be dealt with approximately [18] or using area sources [15] in traditional AEM for the Laplace equation, but are readily handled with, or lead to, the Helmholtz equation.

3 LT-AEM elements

3.1 Taxonomy

Two-dimensional LT-AEM elements can be categorized with respect to:

1. boundary condition and whether element coefficients are prescribed (i.e., "given" in AEM literature);
2. element geometry (e.g. line or area);
3. changes to source terms or constants in the governing equation (e.g. wave number or initial conditions);
4. element time behavior (e.g. constant, square wave, or pulse).

The free parameters for prescribed elements are independent of other elements in the system (e.g. a well with specified pumping rate). Circles, ellipses, and lines usually define regions of different aquifer parameters, and their coefficients must be determined at run-time. Variable time behavior for any type of element is handled in LT-AEM using Laplace-space convolution.
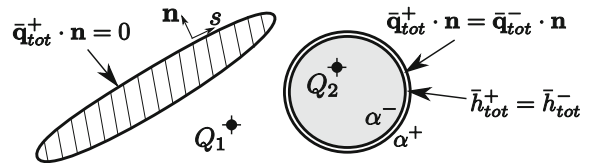
3.2 Boundary conditions

We use boundary-condition matching to determine free coefficients; boundary conditions can be of Dirichlet, Neumann or mixed type. Interface (i.e., matching or continuity) boundary conditions are posed along boundaries between regions defined by 2D elements. A mixed boundary condition along the circumference of an element is

$$\xi \nabla \bar{\Phi} \cdot \mathbf{n} + \zeta \bar{\Phi} = \bar{F}(s, p), \tag{12}$$

where s is the arc length along the boundary. Setting $\xi = 0$, $\zeta = 1$ leaves a Dirichlet boundary condition; $\bar{F}_D(s, p) = K\bar{h}_{\mathrm{BC}}(s, p)$ is the transformed head along the circumference of the element. With $\zeta = 0$, $\xi = 1$, Eq. 12 becomes a Neumann boundary condition; now $\bar{F}_N(s, p) = \bar{q}_{\mathrm{BC}}(s, p)$ is the transformed normal flux on the element boundary.

Fig. 2 Example with no-flow ellipse, prescribed point sources and circular matching element with different α inside and out (+ and − parts of matching element offset for clarity)

Interface boundary conditions are associated with a two-sided element (see circle in Fig. 2); we relate the Neumann and Dirichlet boundary conditions on each side, setting $\bar{F}_N^+(s, p) = \bar{F}_N^-(s, p)$ and $(K^-/K^+)\bar{F}_D^+(s, p) = \bar{F}_D^-(s, p)$, which enforce (6) and (8).

We can specify both a Dirichlet and a Neumann condition along the boundary for an elliptic differential equation because we do not specify a value, but only indicate equality of the inside and outside. Elements that are not interface conditions have their boundary conditions specified in terms of total discharge potential (6) or normal flux, (8); if there are at least two elements, their strengths must be determined simultaneously.

To determine element coefficients, M matching points are chosen along the element boundaries, creating a system of $2M$ equations (M normal flux + M head), for the $2N$, unknowns. We use overspecification [39]; by choosing $2M \geq 2N$, the system of equations is solved in a least-squares sense. Overspecification often produces a smoother solution than $2M = 2N$ does, and for the same M, N is smaller (i.e., the solution does not require the $2M - 2N$ highest-order basis functions). For these reasons it is utilized in the LT-AEM. We use QR decomposition (as done in the LAPACK [40] routine ZGELSS) to solve the least-squares problem, rather than posing the traditional normal equations (e.g. [41, Sect. 5.3] and [42, Chap. 19]).

3.3 Geometric considerations

Table 1 categorizes elements related to Helmholtz-separable 2D coordinates. Elliptical coordinates are the most general 2D coordinates; polar, parabolic, and Cartesian coordinates can be obtained by moving the elliptical foci together or moving one or both of the foci to ∞, respectively. In 2D, singular elements are sources or sinks, while areas are defined by finite boundaries or infinite lines.

3.4 Source terms

Individual elements or entire domains can be governed by differential equations other than (3); they can be completely different (e.g. Laplace's equation) or only differ by material properties or the presence of source terms. Source terms can be either homogeneous (functions of $\bar{\Phi}$) or inhomogeneous (a Poisson term). Homogeneous LT-AEM area sources can be handled without modification to the solution process, since (3) contains this type of term, additional terms only change the definition of κ^2, the wave number. Poisson terms (including Φ_0 in (2)) must be expressed in terms of a particular solution.

Table 1 Helmholtz-separable 2D coordinate systems ([69], [53, Chap. 1], and [33, pp. 655–666])

Coordinate system	Finite boundary	Singular element	Infinite boundary	Modified Helmholtz special functions
Cartesian	*None*	∞ line	∞ line	Exponential
Polar (circular)	Circle	Point	Ray	Modified Bessel
Elliptical	Ellipse	Line segment	Hyperbola	Modified Mathieu
Parabolic	*None*	Semi-∞ line	Parabola	Parabolic cylinder

3.4.1 Homogeneous leaky-aquifer source term

Homogeneous source terms arise from effects that are proportional to changes in head or drawdown in the aquifer. For example, transient leakage from adjacent aquitards, delayed yield in unconfined systems, and dual-domain behavior all lead to homogeneous source terms [4, Sect. 4.2]. Because the 2D LT-AEM does not represent the third dimension explicitly, Neumann boundary conditions with respect to the third dimension (e.g. $\partial \bar{\Phi}/\partial z|_{z=0}$) must be represented as distributed source terms.

Leakage from an adjacent unpumped aquitard leads to a homogeneous distributed source in 2D. We adapt Hantush's modified leaky system [43] to LT-AEM (see Fig. 3). Beginning with (1) but considering a non-zero source term, G, when expressing the system in terms of Φ, and taking the Laplace transform leads to

$$\nabla^2 \bar{\Phi}_1 - \kappa_1^2 \bar{\Phi}_1 + \bar{G} = 0, \tag{13}$$

where subscript 1 indicates the aquifer and 2 the aquitard. Assuming vertical flow in the overlying aquitard (a common assumption when $K_1 \gg K_2$), (3) simplifies to an ordinary differential equation for $\bar{\Phi}_2$,

$$\frac{d^2 \bar{\Phi}_2}{dz^2} - \kappa_2^2 \bar{\Phi}_2 = 0, \tag{14}$$

where the initial value of Φ_2 is zero. The head-matching boundary condition at the aquifer-aquitard interface ($z = 0$) is $\bar{\Phi}_2 = K_2 \bar{\Phi}_1/K_1$, and at the top the aquitard ($z = b_2$) there is a no-drawdown condition, $\bar{\Phi}_2 = 0$ (see case I of Fig. 3). The solution to (14) that satisfies both conditions is

$$\bar{\Phi}_2(z) = \frac{K_2 \bar{\Phi}_1}{K_1} [\cosh \kappa_2 z - \coth \kappa_2 b_2 \ \sinh \kappa_2 z]. \tag{15}$$

Differentiating (15) and evaluating it at $z = 0$ gives the vertical flux from the aquitard at the interface,

$$\bar{G} = \frac{1}{b_1} \left[\frac{\partial \bar{\Phi}_2}{\partial z} \right]_{z=0}, \tag{16}$$

when this is substituted in (13), the governing equation in the aquifer becomes

$$\nabla^2 \bar{\Phi}_1 - \left[\kappa_1^2 + \kappa_2 \frac{K_2}{b_1 K_1} \coth \kappa_2 b_2 \right] \bar{\Phi}_1 = 0. \tag{17}$$

This can be solved using the same solution techniques used for (3) because the new terms in (17) are all constants that redefine the wave number. Since the governing equation in the aquitard is linear with homogeneous initial and boundary conditions, superposition is valid.

Figures 4, 5, and 6 show effects due to a constant-strength finite-radius well source (e.g. [6] and [44, Sect. 4.3.2]), which for (3) is

$$\bar{\Phi}_{\text{well}}(r) = \frac{Q}{2\pi b_1 p} \frac{K_0(r\kappa)}{\kappa r_w K_1(r_w \kappa)}, \tag{18}$$

where K_0 and K_1 are modified Bessel functions (see [30, Sect. 7.2] for properties), r_w is the pumping well radius $[L]$, and Q is the pumping rate $[L^3/T]$. To exploit axial symmetry, the plots show dimensionless results; $t_D = t K_1/(S_{s1} r^2)$ is dimensionless time and $s_D = 4\pi |\Phi - \Phi_0|/Q$ is dimensionless drawdown. The curve labeled $E_1(t_D/4)$ represents the non-leaky Theis solution [45], an exponential integral (see [27, Chap. 5] for properties). The well solution (18) to (17) produces the flattening curves in Fig. 4.

A similar procedure is used to develop a leaky solution with a different aquitard boundary condition; the equation for a no-flow boundary condition at $z = b_2$ is (case II, the upwardly-deviating curves in Fig. 4)

$$\nabla^2 \bar{\Phi}_1 - \left[\kappa_1^2 + \kappa_2 \frac{K_2}{b_1 K_1} \tanh \kappa_2 b_2 \right] \bar{\Phi}_1 = 0. \tag{19}$$

For the thick-aquitard case ($b_2 \to \infty$), $\coth \kappa_2 b_2$ in (17) and $\tanh \kappa_2 b_2$ in (19) simplify to unity (the middle leaky curve in Fig. 4). The effects of the boundary condition at $z = b_2$ are only observed at later time when the three curves separate (the thin curves in Fig. 4 represent an aquitard 1/10 as thick as the heavy curves—they deviate at an earlier time). The effects of two aquitards (above and below) can be included, as done by Hantush [43]. The second aquitard adds another term, analogous to those in (17) and (19).
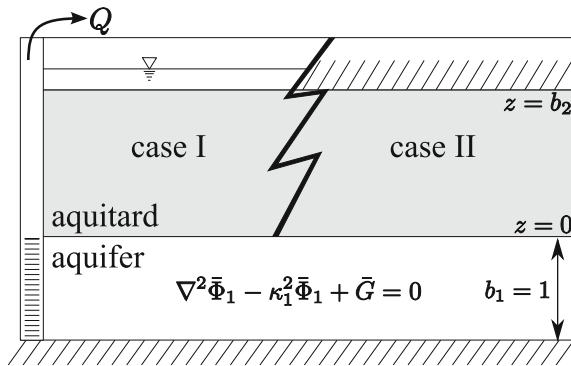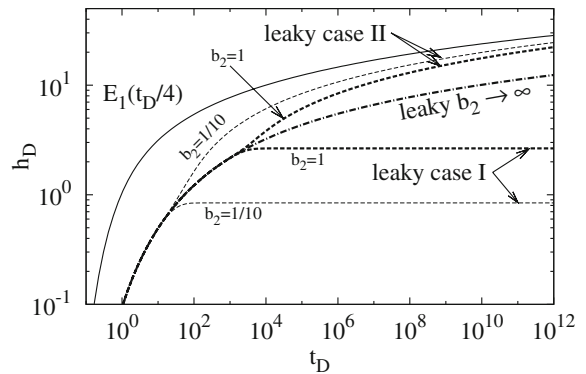
Fig. 3 Leaky system diagram

Fig. 4 Leaky response at $r = 1$ due to point source (18), comparing results for different aquitard boundary conditions and aquitard thicknesses with the non-leaky E_1 solution; $S_{s2}/S_{s1} = 100$, $K_1/K_2 = 5$

3.4.2 Homogeneous source due to extended form of Darcy's law

Higher-order time derivatives in the governing time-domain equation (representing inertia) also lead to a homogeneous source term in the Laplace-domain. The effect of not considering this inertia term, in situations where it may be significant (e.g. the coarse gravel-packed region surrounding a pumping well), may lead to slight over-estimation of storage parameters with diffusion models. Consider the more complete transient form of Darcy's law (averaged from, or through analogy with, the Navier–Stokes equations (e.g. [46, Sect. 5.10.6] and [47, Sect. 1.5.1])), given as

$$\mathbf{q} = -\left(\nabla \Phi + \tau \frac{\partial \mathbf{q}}{\partial t}\right), \tag{20}$$

where τ is the relaxation parameter $[T]$, a property related to the time it takes the system to become diffusion-dominated. Typically τ is small and the time-derivative term is neglected. Löfqvist and Rehbinder [48] define $\tau = K/(ng)$, where n is the dimensionless porosity and g is the acceleration due to gravity $[L/T^2]$. Combining the Laplace-space mass-conservation equation,

$$-\nabla \cdot \bar{\mathbf{q}} - \kappa^2 \bar{\Phi} = 0, \tag{21}$$

with the Laplace transform of (20), the governing equation becomes

$$\nabla \cdot \left[\frac{1}{1 + \tau p} \nabla \bar{\Phi}\right] - \kappa^2 \bar{\Phi} = 0, \tag{22}$$

assuming initial head and flux are zero. This can be put into the form

$$\nabla^2 \bar{\Phi} - \left[\kappa^2 + \tau \frac{p^2}{\alpha}\right] \bar{\Phi} = 0, \tag{23}$$

which is again similar to (3), but with an additional p^2 term in the wave number. Equation (23) can be solved for a point source by redefining the wave number in (18) (see Figs. 5 and 6).

Equation (23) is the transformed damped wave equation, a more general form of the diffusion equation [25, Chap. 8]. For problems governed by the wave equation, pulses always propagate at finite speed (e.g. see steep leading edge of s_D surface in Fig. 6), while the diffusion equation allows changes to propagate at infinite speed [49, Sect. 1.2.1]. For example, $s_D = E_1(t_D/4)$ (Theis's [45] solution) produces non-zero drawdown at every r for $t > 0$; as $r \to \infty$ $s_D \to 0$, so this discrepancy is usually tolerated. In the damped-wave equation τ is inversely proportional to the maximum propagation velocity squared; as $\tau \to 0$, the maximum velocity $\to \infty$, and the damped wave equation becomes the diffusion equation.
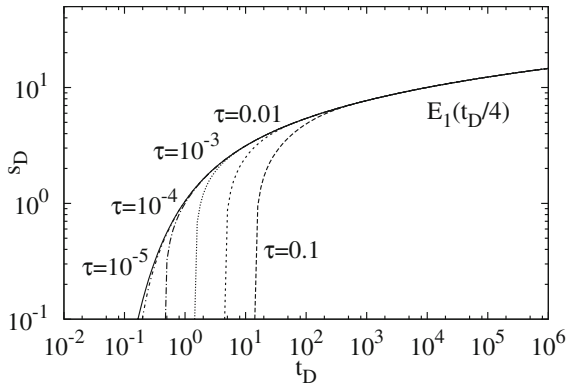
Fig. 5 Time-drawdown at $r = 1$ for point source (18) considering inertia effects
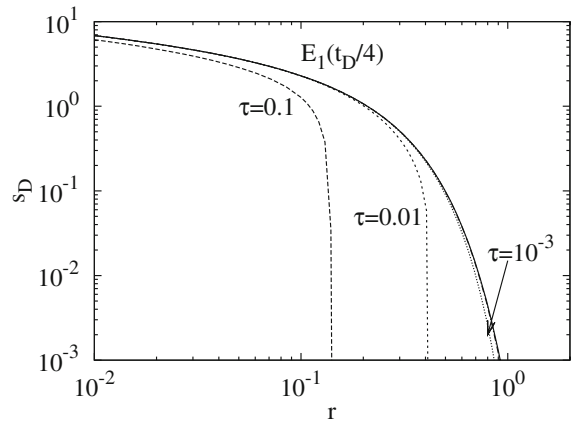

Fig. 6 Distance-drawdown at $t = 0.01$ for point source (18) considering inertia effects

The two distributed source terms discussed in this section are illustrated using (18), but are easily extended to other elements [4, Sect. 4.2]. An elliptical line or area source [22] with a wave number corresponding to a leaky problem is a trivial extension to the existing line or area element, thus analytic solutions to other geometries and superpositions thereof are readily found.

3.4.3 Inhomogeneous source terms

Area sources can be used to represent constant recharge or discharge, or variable recharge where the source term is not proportional to aquifer drawdown. For circular elements, Kuhlman and Neuman [22] showed that $\Phi_0 \neq 0$ can be represented as impulse area sources by decomposing the solution to the inhomogeneous governing equation into a homogeneous and a particular solution [12, Sect. 37].

The particular solution for an initial condition that is linear or constant in space can be found by inspection, since the Laplacian of this type of function has zero contribution to the particular solution. Inhomogeneous terms with more general spatial behavior may be computed numerically using area integration of the Green's function, through variation of parameters using known eigenfunctions, or derived as area sources in general functional forms (e.g. 2D multi-quadric surfaces [50]).

4 Elliptical elements

Circular LT-AEM elements are given by Furman and Neuman [6], while elliptical elements are derived here using an analogous procedure [4, Sect. 3.2]. Bakker [28,51] and Bakker and Nieber [8] derived elliptical AEM elements for the modified Helmholtz equation. A significant difference between their elliptical AEM solutions and that given here is the presence of the complex Laplace parameter, p, which becomes large at small time; this is because p and t are multiplicative arguments to the exponential in the definition of the Laplace transform (e.g. [35, Sect. 4.24] and [26, Chap. 7]).

Elliptical coordinates (see Fig. 7) are defined as $x = f \cosh \eta \cos \psi$ and $y = f \sinh \eta \sin \psi$, where (η, ψ) are dimensionless elliptical coordinates and f is the semi-focal length $[L]$. The transforms are given succinctly in terms of a conformal map; when $z = x + iy$ and $\zeta = \eta + i\psi$, the forward transform is $z = f \cosh \zeta$ and the backward transform is $\zeta = \text{arccosh } z/f$. The multi-valued complex inverse hyperbolic cosine can be expressed as a single-valued function [52] in the form
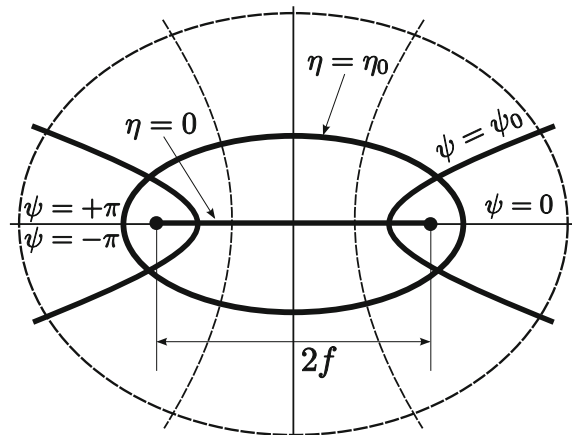
Fig. 7 Components of elliptical coordinates (η, ψ); f is semi-focal distance
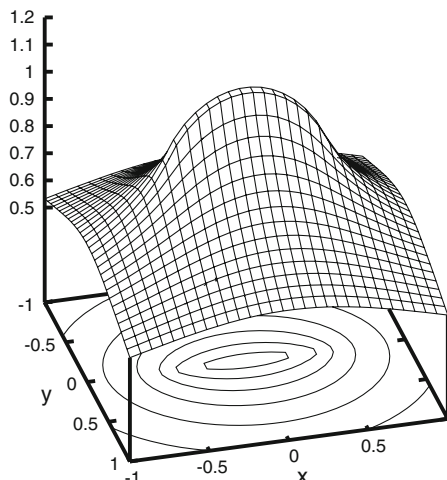

Fig. 8 Constant-strength line source solution for $f = 0.5$, $Q = 1$, $\alpha = 5.0 \times 10^4$, $t = 0.0125$; h contour interval is 0.1

$$
\zeta = \begin{cases} \log\left(z/f + \sqrt{(z/f)^2 - 1}\right) & x > 0, \\ \log\left(z/f - \sqrt{(z/f)^2 - 1}\right) & x \leq 0. \end{cases} \tag{24}
$$

The modified Helmholtz equation (3) in elliptical coordinates (e.g. [31, Chap. 9], [53, p 17], [33, p 1407]) is

$$
\frac{2}{f^2 \left[\cosh 2\eta - \cos 2\psi\right]} \left[\frac{\partial^2 \bar{\Phi}}{\partial \eta^2} + \frac{\partial^2 \bar{\Phi}}{\partial \psi^2}\right] - \kappa^2 \bar{\Phi} = 0, \tag{25}
$$

with the condition that $\bar{\Phi}(\psi) = \bar{\Phi}(\psi + 2\pi)$. Upon substitution of the form $\bar{\Phi}(\eta, \psi) = H(\eta)\Psi(\psi)$, Eq. 25 can be separated into two ordinary differential equations,

$$
\frac{\mathrm{d}^2 \Psi}{\mathrm{d}\psi^2} + (\omega - 2q \cos 2\psi)\, \Psi = 0, \tag{26a}
$$

$$
\frac{\mathrm{d}^2 H}{\mathrm{d}\eta^2} - (\omega - 2q \cosh 2\eta)\, H = 0, \tag{26b}
$$

where ω is a separation constant (Mathieu characteristic number a or b in Mathieu-function literature) and $q = -f^2 \kappa^2 / 4$ is the Mathieu parameter. These are the angular (26a) and radial (26b) Mathieu equations. The parameter q is specified through the aquifer properties, element geometry, and p, while ω is determined to make the solution to (26a) periodic on $\pi \leq \psi < -\pi$. The special functions that are solutions to (26a) and (26b) are Mathieu functions; see [8,54,55] for characteristic functional plots. Solutions to (25) for $\mathfrak{Re}(q) < 0$ are

$$
\bar{\Phi}_e^+(\eta, \psi) = \sum_{n=0}^{\infty} a_n \, \mathrm{Ke}_n(\eta; -q) \, \mathrm{ce}_n(\psi; -q) + \sum_{n=1}^{\infty} b_n \, \mathrm{Ko}_n(\eta; -q) \, \mathrm{se}_n(\psi; -q), \tag{27a}
$$

$$
\bar{\Phi}_e^-(\eta, \psi) = \sum_{n=0}^{\infty} c_n \, \mathrm{Ie}_n(\eta; -q) \, \mathrm{ce}_n(\psi; -q) + \sum_{n=1}^{\infty} d_n \, \mathrm{Io}_n(\eta; -q) \, \mathrm{se}_n(\psi; -q), \tag{27b}
$$

where a_n, b_n, c_n and d_n are the coefficients to be determined; Ie_n, Io_n, Ke_n, and Ko_n are the even (e) and odd (o) radial Mathieu function of first and second kind, and ce_n and se_n are the even (cosine-elliptic) and odd (sine-elliptic) first-kind angular Mathieu function. Equation (27a) only contains the second-kind radial Mathieu functions

(Ke$_n$, Ko$_n$) which are finite as $\eta \to \infty$. Similarly, Eq. 27b only contains the first-kind radial Mathieu function (Ie$_n$, Io$_n$) that has continuous value and slope across the focal line, $\eta = 0$. Because $\mathfrak{Re}(q) < 0$, these are modified Mathieu functions.

To simplify the expression for head matching (6) on the boundary of the ellipse, the radial Mathieu functions are normalized, resulting in

$$\bar{\Phi}_e^+(\eta \geq \eta_0, \psi) \approx \sum_{n=0}^{N-1} a_n \frac{Ke_n(\eta; -q^+)}{Ke_n(\eta_0; -q^+)} ce_n(\psi; -q^+) + \sum_{n=1}^{N-1} b_n \frac{Ko_n(\eta; -q^+)}{Ko_n(\eta_0; -q^+)} se_n(\psi; -q^+), \tag{28a}$$

$$\bar{\Phi}_e^-(\eta \leq \eta_0, \psi) \approx \sum_{n=0}^{N-1} c_n \frac{Ie_n(\eta; -q^-)}{Ie_n(\eta_0; -q^-)} ce_n(\psi; -q^-) + \sum_{n=1}^{N-1} d_n \frac{Io_n(\eta; -q^-)}{Io_n(\eta_0; -q^-)} se_n(\psi; -q^-), \tag{28b}$$

where the infinite sum has been truncated and the $\pm$ superscripts on q indicate whether it involves aquifer parameters from inside ($-$) or outside ($+$) the ellipse $\eta = \eta_0$. In polar coordinates, a similar set of expressions is derived [6,16]; they are

$$\bar{\Phi}_c^+(r \geq r_0, \theta) \approx \gamma_0 \frac{K_0(r\kappa^+)}{K_0(r_0\kappa^+)} + \sum_{n=1}^{N-1} \frac{K_n(r\kappa^+)}{K_n(r_0\kappa^+)} \left[\gamma_n \cos(n\theta) + \delta_n \sin(n\theta) \right]. \tag{29}$$

The first difference between (29) and (28a) is the "even" and "odd" radial functions in elliptical coordinates. A second difference is the appearance of both an argument (η or ψ) and a parameter, $q^\pm$, in (28a) and (28b). Thirdly, both radial and angular Mathieu functions depend on the coefficients of the partial differential equation (through q), while sine and cosine in (29) do not.

4.1 Line source

An expression for a constant-flux line source (along $y = 0$, from $-f \leq x \leq f$) is obtained from (27a), using only ce$_{2n}(\psi; -q)$ due to symmetry . To simplify flux matching (8) we normalize by the radial Mathieu function derivative, Ke$'_{2n}(0; -q)$, giving

$$\bar{\Phi}_{line}(\eta, \psi) = \sum_{n=0}^{\infty} \beta_{2n} ce_{2n}(\psi; -q) \frac{Ke_{2n}(\eta; -q)}{Ke'_{2n}(0; -q)}, \tag{30}$$

where β_{2n} are the coefficients to be determined. The boundary condition for a specified flux line element in elliptical coordinates is

$$\bar{q}_{BC} = \bar{g}(p) \frac{\bar{\lambda}}{2f} = -\frac{1}{f\sqrt{\frac{1}{2}(\cosh 2\eta - \cos 2\psi)}} \frac{\partial \bar{\Phi}_{line}}{\partial \eta} \bigg|_{\eta=\eta_0}, \tag{31}$$

where $\bar{\lambda}$ is the transformed constant flowrate $[L^3]$, $2f$ is the length of the line segment, and $\bar{q}_{BC}$ is the normal flux $[L]$ due to the line source. The metric coefficient in the denominator is required to preserve the correct dimensions [33, Sect. 1.3]. Differentiating (30) with respect to η, evaluating it at $\eta = 0$, and using orthogonality over $0 < \psi < \pi$ gives

$$-\bar{g}(p) \frac{\bar{\lambda}}{2} \int_0^\pi \sin \psi \, ce^*_{2m}(\psi; -q) \, d\psi = \sum_{n=0}^{\infty} \beta_{2n} \int_0^\pi ce_{2n}(\psi; -q) \, ce^*_{2m}(\psi; -q) \, d\psi, \tag{32}$$

where ce$_{2m}(\psi; -q)$ has period π and $*$ denotes the complex conjugate. Due to the orthogonality of the angular Mathieu functions, the integral on the right in (32) is 0 for $m \neq n$ and is defined as $\pi/2$ for $m = n$ [31, Sect. 2.19], reducing the infinite sum to the $2m$th term. The expression for the coefficients is

$$\beta_{2m} = -\bar{g}(p) \frac{\bar{\lambda}}{\pi} \int_0^\pi ce^*_{2m}(\psi; -q) \sin \psi \, d\psi. \tag{33}$$
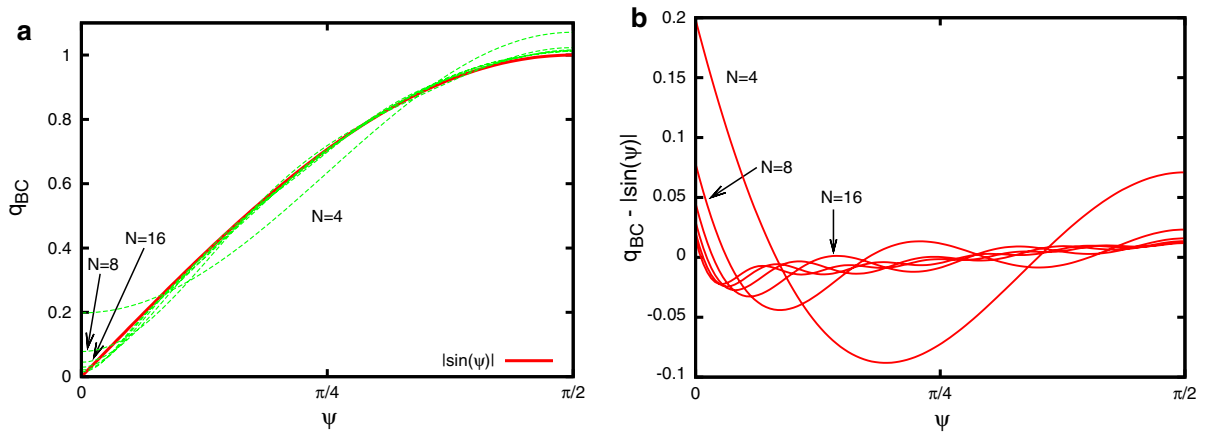
Fig. 9 Flux boundary condition and error in Mathieu function expansion for line source in Fig. 8

Expanding ce^*_{2m} in terms of its defining infinite cosine series (A1a), and evaluating the resulting integral leaves

$$\beta_{2m} = \bar{g}(p) \frac{2\bar{\lambda}}{\pi} (-1)^{m+1} \left[\sum_{r=0}^{\infty} (-1)^r \frac{A_{2r}^{(2m)*}}{1 - (2r)^2} \right], \tag{34}$$

where $A_{2r}^{(2m)}$ is a matrix of Mathieu coefficients (see Appendix A). The terms in the infinite sum quickly become small as r increases and the largest magnitude terms in $A_{2r}^{(2m)}$ occur surrounding the diagonal $r = m$ (as $q \to 0$, $A_{2r}^{(2m)}$ becomes a diagonal matrix). Substituting (34) back in (30) gives the final expression for a constant strength passive line source as

$$\bar{\Phi}_{line}(\eta, \psi) = \bar{g}(p) \frac{4\bar{\lambda}}{\pi} \sum_{n=0}^{\infty} (-1)^{n+1} \left[\sum_{r=0}^{\infty} (-1)^r \frac{A_{2r}^{(2n)*}}{1 - (2r)^2} \right] ce_{2n}(\psi; -q) \frac{Ke_{2n}(\eta; -q)}{Ke'_{2n}(0; -q)}. \tag{35}$$

This formulation of the transient line source is valid for any-length line source and can take on different time behaviors through convolution with various $\bar{g}(p)$. Figure 8 illustrates the solution for $\bar{g}(p) = 1/p$ (a constant strength starting at $t = 0$), using $M = 20$ and an infinite matrix for the Mathieu functions truncated at 42 terms. Tranter [56] derived a real-valued Mathieu function solution for the case of an ellipse with a Dirichlet boundary condition. Kucûk and Brigham [57] applied Tranter's solution to flow in anisotropic petroleum reservoirs, and Riley [58] derived expression for flow in a petroleum reservoir to a linear crack. Kuhlman and Warrick [20] derived a Mathieu function solution for linearized infiltration from an ellipse. Morse and Feshbach [33, pp. 1419–1425] give a solution in terms of Mathieu functions for a Neumann boundary condition similar to flow through a slot, with real and positive q, while Erricolo [59] shows how these types of series can be accelerated to minimize the number of Mathieu-function evaluations.

The flux normal to the line source at $\eta = 0$, illustrated in Fig. 8, is compared to the true boundary condition in Fig. 9 for increasing numbers of terms in the Mathieu-function expansion. The numerically integrated average error, along the boundary of the element, is 0.011 for $N = 4$ and reduces to -3.6×10^{-3} for $N = 12$; the average error decreases slowly beyond that as more terms are added. The solution converges slowest at the ends of the interval, where the even function $ce_{2n}(\psi)$ must force the flux to zero.

An ellipse or line element expressed in elliptical coordinates using Mathieu functions is useful as an LT-AEM element with the coefficients of (27a) determined at run time or as an element for the special case of strength constant in space (35). Using approximate methods, rather than the appropriate eigenfunctions, may be better suited for intersecting line elements; similar to those in [28], but using an approximation can accommodate large p values accurately.

5 Numerical inverse Laplace transform

Complex contour-integration techniques could be used to analytically compute the time-domain solution from the Mellin contour integral (e.g. [21, Sect. 66] and [44, Sect. 3.2]), defined as

$$\Phi(\mathbf{x}, t) = \mathcal{L}^{-1} \left\{ \bar{\Phi}(\mathbf{x}, p) \right\} = \frac{1}{\mathrm{i}2\pi} \int_{\sigma_0 - \mathrm{i}\infty}^{\sigma_0 + \mathrm{i}\infty} \bar{\Phi}(\mathbf{x}, p) e^{pt} \, \mathrm{d}p, \tag{36}$$

where $\sigma_0 \geq 0$ is larger than the real part of the right-most singularity in $\bar{\Phi}(\mathbf{x}, p)$. Analytic inversion techniques (e.g. method of residues) are very problem-specific and may only yield a solution in the form of a slowly converging infinite series; using a numerical $\mathcal{L}^{-1}$ allows flexibility and generality. See [36, Chap. 9], and the references therein, for general reviews and comparisons of popular numerical numerical inverse Laplace-transform algorithms; Kuhlman [4, Chap. 5] discusses the details related to several alternative inverse methods in the context of the LT-AEM.

A set of LT-AEM solutions are computed for required values of p, whose optimum values depend on the algorithm being used. The time-domain solution is then approximated from this set using a numerical inverse-Laplace-transform algorithm. Furman and Neuman [6] utilized the doubly accelerated Fourier-series approach of de Hoog et al. [60], but no method is universally best. The Fourier-series method can accurately invert an LT-AEM solution over a log-cycle of t values for a set of p optimized for $t_{\max}$ (the largest t desired). The unaccelerated form of the Fourier-series algorithm is [37, Chap. 19],

$$\Phi(t) \approx \frac{e^{\sigma t}}{T} \sum_{k=0}^{2M}{}' \, \Re\mathfrak{e} \left[\bar{\Phi} \left(\sigma + \frac{\mathrm{i}\pi k}{T} \right) \exp \left(\frac{\mathrm{i}\pi t}{T} \right) \right], \tag{37}$$

where T is a scaling parameter (typically $2t_{\max}$); the first and last terms in the summation are halved, and σ depends on the locations of the singularities in $\bar{\Phi}$. The argument of $\bar{\Phi}$, the results of the Laplace-space LT-AEM, are not directly a function of the desired time being inverted, although the optimal value of T is dependent on $t_{\max}$. Choosing $M \geq 20$ will successfully invert most time behaviors over a log-cycle of time (e.g. two discontinuities in $g(t)$, representing turning a pumping well on and off), but a smaller M can be used (as low as $M = 3$ for smooth functions) when T is chosen optimally for each value of time, rather than inverting a whole log-cycle of times at once.

Other algorithms sample the Laplace-space function in different ways. Not all numerical inverse-Laplace-transform algorithms are appropriate, depending on problem-specific restrictions on $\bar{\Phi}$ (e.g. real valued only, or invalid for $\Re\mathfrak{e}(p) < 0$).

6 Example: leaky circles

We simulate six circular regions where κ^2 corresponds to a leaky problem (Case I, (17)); they are surrounded by material with a wave number $\kappa^2 = p/\alpha$ (Fig. 10). A point source at $(-0.5, 0)$, in the background of the leaky circles, is pumped at a constant rate, starting at $t = 0$. The circles represent permeable regions in an otherwise impermeable aquiclude separating two aquifers, the upper aquifer being at constant head. The initial and far-field conditions are $\Phi(r, 0) = \lim_{r \to \infty} \Phi(r, t) = 0$. Contours of h are logarithmically spaced between -0.01 and -10. The pumped aquifer has the same properties everywhere, but the wave number is different inside the circles, representing the effects of an aquitard with the properties: $K_2 = K_1/2$, $S_{s2} = (5 \times 10^3)S_{s1}$, $b_2 = 2$. Twelfth-order eigenfunction approximations and 41 values ($M = 20$ in (37)) of p were used to compute the solution in Figs. 10 and 11.

The effects of the leaky circles are clear in the contour plot; the circles behave as area sources, with their recharge rate proportional to the drawdown in the aquifer. The circles "bend" the h contours, reducing the drawdown compared to the non-leaky case.

Figure 11 shows drawdown observed at points A $(0.5, 0)$ and B $(1.75, 0)$ through time, located in Fig. 10. The upper curve represents Theis's solution [45] (entire domain non-leaky) and the lower solid curves represent Hantush's solution [43] (whole domain leaky). The curves representing the domain with discontinuous leaky layers
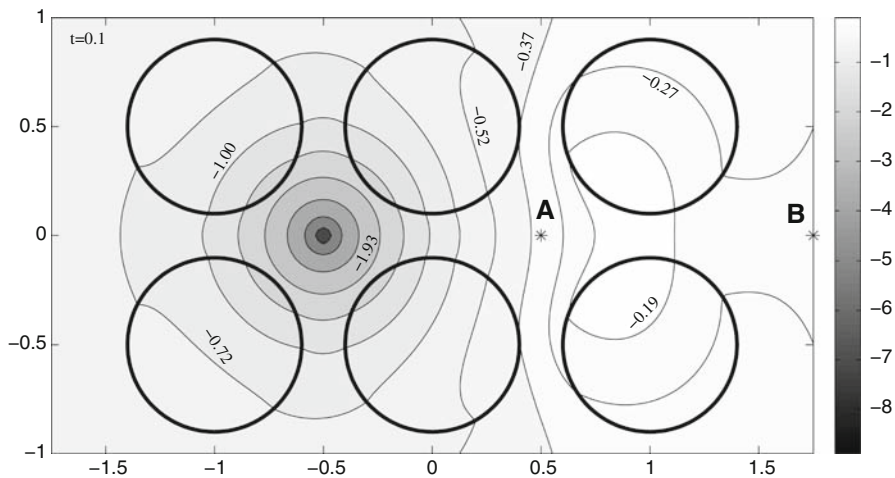
Fig. 10 h contours due to a point source at $(-0.5, 0.0)$ and six case I leaky circular elements (circles represent boundaries of leaky regions) at $t = 0.1$. The aquifer surrounding the circles is non-leaky

Fig. 11 Time-drawdown at two points (see Fig. 10 for locations), showing the effects of leaky circles (thick dashed lines) compared to Theis's (E_1, non-leaky) and Hantush's (thin solid lines, uniformly leaky) solutions
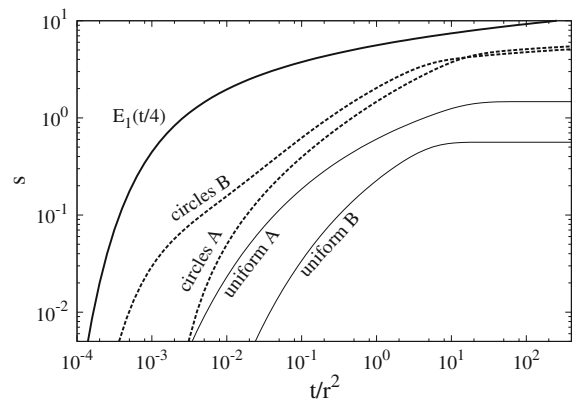
(dashed lines) plot between these two extremes. When the entire domain is leaky, a steady state is reached. With only leaky circles, the drawdown does not completely flatten out in the figure, the time when the near-steady portion is reached is shifted compared to Hantush's solutions. For the circles, the approximate steady-state is approached at a higher value of drawdown, which produces a larger flux from the aquitard, to compensate for the smaller area producing flux to the aquifer.

7 Conclusions

AEM and LT-AEM lie between analytic solutions and gridded models in terms of flexibility and accuracy; they extend some of the elegance of analytic solutions to a broader set of geometries. LT-AEM additionally utilizes the Laplace transform to achieve flexible analytic temporal behavior through convolution, while retaining the benefits of AEM.

The eigenfunction-expansion approach is an elegant method for deriving flexible semi-analytic solutions for some geometries. Complex non-separable geometries can be approached using approximate techniques borrowed from the boundary- and spectral-element literature. As examples, the LT-AEM approach was extended to two problems of potential interest to hydrologists, which are easily solvable using the same solution techniques used for the standard LT-AEM. These new leaky and damped-wave solutions exemplify how LT-AEM can be extended to more

general aquifer test-analysis scenarios; unconfined, dual porosity, and multi-aquifer flow may be similarly handled [4, Sect. 4.2].

Sections 3.4.1 and 3.4.2 illustrate the potential usefulness of LT-AEM for interpreting observed results from aquifer tests. The inhomogeneous example (Figs. 10 and 11) illustrates how LT-AEM has flexibility not found in standard analytic aquifer-flow solutions and both elegance and insight lacking from gridded numerical solutions. Future and ongoing extension of LT-AEM to three-dimensional flow (i.e., cylindrical and rotational 3D coordinates), elements with anisotropic material properties (e.g. K is not a scalar), the inclusion of transient particle tracking, the addition of more aquifer test related elements (e.g. elements with unconfined behavior, wellbore storage, or a skin), and the addition of approximate elements will increase the flexibility and usefullness of LT-AEM.

While the nomenclature and examples used here are given in terms of hydrogeology, LT-AEM would also be useful for the solution of heat conduction, neutron scattering, and other diffusion-dominated processes. The extension to the damped-wave problem also shows that LT-AEM has the ability to solve additional problems which can be transformed into the modified Helmholtz equation using the Laplace transform, which includes other non-diffusion wave-like processes.

Appendix A: Mathieu functions

To compute Mathieu functions of complex argument, the matrix formulation of the eigenvalue problem is used here [61–64], solved with LAPACK [40] routine ZGEEV. The traditional continued-fraction approach to solving for the eigenvalues [65] is potentially more efficient than the matrix method, but it requires an initial guess and is only valid for small Mathieu parameter, $|q| \leq 4n$, with asymptotic relationships required for larger q (e.g. [66,67] and [68, Chap. 5]). The matrix used to compute the eigenvalues, ω, and eigenvectors, A_r^n and B_r^n, is a truncated infinite matrix, obtained by substituting the definitions of the angular Mathieu functions back in (26a); the size of the matrix required is in general proportional to the highest order of Mathieu function needed, the accuracy desired, and $|q|$ [62,63].

With either the matrix or continued-fraction approach, when the Mathieu parameter takes on complex values, pairs of eigenvalues (and their associated eigenvectors) degenerate at isolated branch points (double points) in the complex q-plane. References [65] and [67] discuss the location of and ramification of these double points.

This degeneracy results in the pairs of eigenvectors being less than orthogonal, depending on the value of q (numerically, the eigenvectors are not likely to be exactly degenerate). This behavior is not a problem for the overall convergence of the solution when a more general QR least-squares solution (e.g. LAPACK routine ZGELSS) is used, which can accommodate this occasional degeneracy. Numerical inverse-Laplace-transform methods utilize a set of $\bar{\Phi}(\mathbf{x}, p)$ to compute the time-domain solution. If an entry in this set coincides with a double point of Mathieu's equation, there will be two non-orthogonal eigenvectors. Because this degeneracy only affects a pair of the N eigenvectors at one (or possibly two) of the values of p, it is not critical to the overall performance of the method.

Angular Mathieu functions are evaluated from their definitions in terms of infinite sine and cosine series (second-kind non-period angular Mathieu functions are not useful in our application), for $\mathfrak{Re}(q) < 0$ they are:

$$\text{ce}_{2n}(\psi; -q) = (-1)^n \sum_{r=0}^{\infty} (-1)^r A_{2r}^{(2n)} \cos(2r\psi), \tag{A1a}$$

$$\text{ce}_{2n+1}(\psi; -q) = (-1)^n \sum_{r=0}^{\infty} (-1)^r B_{2r+1}^{(2n+1)} \cos[(2r+1)\psi], \tag{A1b}$$

$$\mathrm{se}_{2n+1}(\psi;-q) = (-1)^n \sum_{r=0}^{\infty} (-1)^r A_{2r+1}^{(2n+1)} \sin[(2r+1)\psi], \tag{A1c}$$

$$\mathrm{se}_{2n+2}(\psi;-q) = (-1)^n \sum_{r=0}^{\infty} (-1)^r B_{2r+2}^{(2n+2)} \sin[(2r+2)\psi], \tag{A1d}$$

where $A_r^{(n)}$ and $B_r^{(n)}$ are matrices of Mathieu coefficients (both functions of q); each is comprised of the eigenvectors associated with the nth eigenvalue that provides a periodic solution to angular Mathieu equation. Even-order ($2n$ and $2n+2$) Mathieu functions are periodic in π, while odd-order Mathieu functions are 2π periodic.

Because eigenvectors only define a direction, their lengths must be normalized. An extension of McLachlan's normalization [31, Sect. 2.21] is used, since it is readily generalized to the complex case and it produces angular Mathieu function of root mean squared value $1/\sqrt{2}$ over the entire range of ψ (LAPACK subroutine ZGEEV returns this scaling, additionally scaling the largest magnitude element of each vector to be real). The Mathieu coefficients are normalized by $\int_{-\pi}^{\pi} \mathrm{ce}_n^*(\psi;-q)\mathrm{ce}_n(\psi;-q)\mathrm{d}\psi = \int_{-\pi}^{\pi} \mathrm{se}_n^*(\psi;-q)\mathrm{se}_n(\psi;-q)\mathrm{d}\psi = \pi$, where $*$ denotes the complex conjugate; this makes Mathieu functions degenerate to trigonometric functions as $q \to 0$.

Radial Mathieu functions are best defined in terms of Bessel-function product series (convergent for all η). Expressions for them are lengthy, and can be found in the literature [31, Sect. 13.30]. References [27, p 744] and [55] have tables relating these functions' various names found in different publications. Derivatives of Mathieu functions are found by applying the derivative to the definitions; no recurrence relationships exist.

References

1. Kraemer SR (2007) Analytic element ground water modeling as a research program (1980 to 2006). Ground Water 45(4):402–408
2. Strack ODL, Haitjema HM (1981) Modeling double aquifer flow using a comprehensive potential and distributed singularities 1. Solution for homogeneous permeability. Water Resour Res 17(5):1535–1549
3. Boyd JP (2000) Chebyshev and Fourier spectral methods. 2nd ed. Dover Publications, New York
4. Kuhlman KL (2008) Laplace transform analytic element method. VDM Verlag, Saarbrücken
5. Fitts CR (1991) Modeling three-dimensional flow about ellipsoidal inhomogeneities with application to flow to a gravel-packed well and flow through lens-shaped inhomogeneities. Water Resour Res 27(5):815–824
6. Furman A, Neuman SP (2003) Laplace-transform analytic element solution of transient flow in porous-media. Adv Water Res 26(12):1229–1237
7. Bakker M, Strack ODL (2003) Analytic elements for multiaquifer flow. J Hydrol 271(1–4):119–129
8. Bakker M, Nieber JL (2004) Two-dimensional steady unsaturated flow through embedded elliptical layers. Water Resour Res 40(12):W12406
9. Hunt RJ (2006) Ground water modeling applications using the analytic element method. Ground Water 44(1):5–15
10. Strack ODL (1999) Principles of the analytic element method. J Hydrol 226(3–4):128–138
11. Strack ODL (2003) Theory and applications of the analytic element method. Rev Geophys 41(2):1005–1021
12. Strack ODL (1989) Groundwater mechanics. Prentice-Hall, Englewood Cliffs
13. Haitjema HM (1995) Analytic element modeling of groundwater flow. Academic Press, London
14. Haitjema HM, Strack ODL (1985) An initial study of thermal energy storage in unconfined aquifers. Technical report PNL-5818 UC-94e, Pacific Northwest Laboratories
15. Zaadnoordijk WJ, Strack ODL (1993) Area sinks in the analytic element method for transient groundwater flow. Water Resour Res 29(12):4121–4129
16. Butler JJ, Liu W (1993) Pumping tests in nonuniform aquifers: the radially asymmetric case. Water Resour Res 29(2):259–269
17. Bakker M (2004) Transient analytic elements for periodic Dupuit–Forchheimer flow. Adv Water Resour 27(1):3–12
18. Strack ODL (2006) The development of new analytic elements for transient flow and multiaquifer flow. Ground Water 44(1):91–98
19. Bakker M, Nieber JL (2004) Analytic element modeling of cylindrical drains and cylindrical inhomogeneities in steady two-dimensional unsaturated flow. Vadose Zone J 3(3):1038–1049
20. Kuhlman KL, Warrick AW (2008) Quasilinear infiltration from an elliptical cavity. Adv Water Resour 31(8):1057–1065
21. Churchill RV (1972) Operational Mathematics 3rd edn. McGraw-Hill, New York
22. Kuhlman KL, Neuman SP (2006) Recent advances in Laplace transform analytic element method (LT-AEM) theory and application to transient groundwater flow. In: Computational methods in water resources, vol XVI
23. Duffin RJ (1971) Yukawan potential theory. J Math Anal Appl 35(1):105–130

24. Graff KF (1991) Wave motion in elastic solids. Dover Publications, New York
25. Moore RK (1964) Wave and diffusion analogies. McGraw-Hill, New York
26. Özişik NM (1993) Heat conduction. 2nd ed. Wiley-Interscience, New York
27. Abramowitz M, Stegun IA (eds) (1964) Handbook of mathematical functions with formulas, graphs and mathematical tables. Number 55 in Applied Mathematics Series. National Bureau of Standards
28. Bakker M (2004) Modeling groundwater flow to elliptical lakes and through multi-aquifer elliptical inhomogeneities. Adv Water Resour 27(5):497–506
29. Smith BF, Bjorstad PE, Gropp W (1996) Domain decomposition. Cambridge University Press, Cambridge
30. Andrews LC (1998) Special functions of mathematics for engineers. 2nd ed. SPIE Press, Bellingham
31. McLachlan NW (1947) Theory and application of Mathieu functions. Oxford University Press, Oxford
32. Arscott FM (1981) Ordinary and partial differential equations. In: Everitt WN, Sleeman BD (eds) Lecture notes in mathematics, vol 846. The land beyond Bessel: a survey of higher special functions. Springer, Heidelberg
33. Morse PM, Feshbach H (1953) Methods of theoretical physics. vols 1 and 2. McGraw-Hill, New York
34. Oleksy Cz (1996) A convergence acceleration method for Fourier series. Comput Phys Commun 96(1):17–26
35. Lanczos C (1988) Applied analysis. Dover Publications, New York
36. Cohen AM (2007) Numerical methods for Laplace transform inversion. Springer, Heidelberg
37. Davies B (2002) Integral transforms and their application. 3rd ed. Springer, Heidelberg
38. Abate J, Valkò PP (2003) Multi-precision Laplace transform inversion. Int J Numer Methods Eng 60(5):979–993
39. Janković I, Barnes R (1999) High-order line elements in modeling two-dimensional groundwater flow. J Hydrol 226(3–4):211–223
40. Anderson, E, Bai Z, Dongarra J, Greenbaum A, McKenney A, Du Croz J, Hammarling S, Demmel J, Bischof C, Sorensen D (1990) LAPACK: a portable linear algebra library for high-performance computers. In: Proceedings of the 1990 ACM/IEEE conference on supercomputing. IEEE Computer Society, pp 2–11
41. Golub GH, van Loan CF (1996) Matrix computations. 3rd ed. Johns Hopkins University Press, Baltimore
42. Lawson CL, Hanson RJ (1974) Solving least squares problems. SIAM, Philadelphia
43. Hantush MS (1960) Modification of the theory of leaky aquifers. J Geophys Res 65(11):3713–3725
44. Lee T-C (1999) Applied mathematics in hydrogeology. CRC Press, Boca Raton
45. Theis CV (1935) The relation between lowering of the piezometric surface and the rate and duration of discharge of a well using ground-water storage. Trans Am Geophys Union 16(2):519–524
46. Bear J (1988) Dynamics of fluids in porous media. Dover Publications, New York
47. Nield DA, Bejan A (2006) Convection in porous media. 3rd ed. Springer, Heidelberg
48. Löfqvist T, Rehbinder G (1993) Transient flow towards a well in an aquifer including the effect of fluid inertia. Appl Sci Res 51(3):611–623
49. Vásquez JL (2007) The porous medium equation: mathematical theory. Oxford University Press, Oxford
50. Strack ODL, Janković I (1999) A multi-quadric area-sink for analytic element modeling of groundwater flow. J Hydrol 226(3–4):299–196
51. Bakker M (2008) Derivation and relative performance of strings of line elements for modeling (un)confined and semi-confined flow. Adv Water Resour 31(6):906–914
52. Suribhatla RM, Bakker M, Bandilla K, Janković I (2004) Steady two-dimensional groundwater flow through many elliptical inhomogeneities. Water Resour Res 40(4):W04202
53. Moon P, Spencer DE (1961) Field theory handbook: including coordinate systems differential equations and their solutions. Springer-Verlag, Heidelberg
54. Alhargan FA (2000) Algorithm 804: subroutines for the computation of Mathieu functions of integer order. ACM Trans Math Software 26(3):408–414
55. Gutiérrez Vega JC, Rodriguez Dagnino RM, Meneses Nava AM, Chávez Cerda S (2003) Mathieu functions, a visual approach. Am J Phys 71(3):233–242
56. Tranter CJ (1951) Heat conduction in the region bounded internally by an elliptical cylinder and an analogous problem in atmospheric diffusion. Q J Mech Appl Math 4(4):461–465
57. Kucûk F, Brigham WE (1979) Transient flow in elliptical systems. Soc Petroleum Eng J 267:401–410
58. Riley MF (1991) Finite conductivity fractures in elliptical coordinates. PhD thesis, Stanford University
59. Erricolo D (2003) Acceleration of the convergence of series containing Mathieu functions using Shanks transformations. IEEE Antennas Wirel Propag Lett 2:58–61
60. de Hoog FR, Knight JH, Stokes AN (1982) An improved method for numerical inversion of Laplace transforms. SIAM J Stat Comput 3(3):357–366
61. Chaos-Cador L, Ley-Koo E (2002) Mathieu functions revisited: matrix evaluation and generating functions. Rev Mex Fis 48(1):67–75
62. Delft Numerical Analysis Group (1973) On the computation of Mathieu functions. J Eng Math 7(1):39–61
63. Green DJ, Michaelson S (1965) Series solution of certain Sturm-Liouville eigenvalue problems. Comput J 7(4):322–336
64. Stamnes JJ, Spjelkavik B (1995) New method for computing eigenfunctions (Mathieu functions) for scattering by elliptical cylinders. Pure Appl Opt 4(3):251–262
65. Blanch G, Clemm DS (1969) Mathieu's equation for complex parameters: tables of characteristic values. Technical report, Aerospace Research Laboratories, US Air Force

66. Alhargan FA (2000) Algorithms for the computation of all Mathieu functions of integer orders. ACM Trans Math Software 26(3):390–407
67. Hunter C, Guerrieri B (1981) The eigenvalues of Mathieu's equation and their branch points. Stud Appl Math 64:113–141
68. Arscott FM (1964) Periodic differential equations. Macmillan, New York
69. Arscott FM, Darai A (1981) Curvilinear co-ordinate systems in which the Helmholtz equation separates. IMA J Appl Math 27(1):33–70